Journal of Alloys and Compounds 521 (2012) 16–29

Contents lists available at SciVerse ScienceDirect

Journal of Alloys and Compounds

journal homepage: www.elsevier.com/locate/jallcom

Interaction mechanisms between slurry coatings and solid oxide fuel cell interconnect alloys during high temperature oxidation

Å.H. Persson [a,*], L. Mikkelsen [a,1], P.V. Hendriksen [a,2], M.A.J. Somers [b]

[a] Division of Fuel Cells and Solid State Chemistry, Risø National Laboratory for Sustainable Energy, Technical University of Denmark, P.O. 49, DK-4000 Roskilde, Denmark
[b] Department of Mechanical Engineering, Technical University of Denmark, Kemitorvet b.204, DK-2800 Lyngby, Denmark

ARTICLE INFO

Article history:
Received 28 October 2011
Received in revised form
16 December 2011
Accepted 19 December 2011
Available online 20 January 2012

Keywords:
Oxidation
Microstructure
Diffusion
Surfaces and interfaces
Fuel cells
Coating materials

ABSTRACT

Six different coatings consisting of fluorite-, corundum-, spinel- or perovskite-type oxides were deposited on a Fe22Cr alloy (Crofer 22APU) and oxidized at 900 °C in moisturized air.

Five of the coatings prevented break-away oxidation otherwise observed for the uncoated alloy, and the parabolic oxidation rate constant was reduced with 50–90% of that for uncoated alloy. One coating consisting of $MnCo_2O_4$ did not significantly affect the oxidation rate of the alloy, and just as for uncoated samples break-away oxidation occurred for $MnCo_2O_4$ coated samples. The interaction mechanisms between the growing oxide scales and applied coatings can be classified according to three types.

1. Introduction

In a solid oxide fuel cell (SOFC)-stack the interconnect is the component in-between the cathode of one fuel cell and the anode of the next fuel cell. The interconnect also separates the air from the fuel in adjoining cells of a stack. The interconnect material has to be chemically and thermally compatible with the other cell components from room temperature up to operational temperature of the fuel cells, approximately 750–850 °C [1]. Ferrous Cr_2O_3 (chromia) forming alloys have shown promising results as interconnect materials. They are cheap, easy to shape and handle and they meet many of the requirements on interconnect plates including high electrical conductivity, gas tightness, and matching thermal expansion with the cell. Chromia-forming alloys present a good balance between a slow growth rate of the oxide scale and electrical conductivity of the oxide scale in comparison to alumina and silica forming alloys, which have a significantly higher electrical resistance in the forming oxide scale [1–4]. However, for the SOFC-stack to present satisfying operational efficiency the growth rates and the electrical resistance of the oxide scale have to be decreased even further. It would further be beneficial if the chromium content in the protecting oxide scale would be decreased, since chromium species evaporating or diffusing via surfaces from the chromia scale, have a detrimental poisonous effect on the fuel cell. The chromium species tend to diffuse into the cathode/electrolyte interface, where the chromium species block the catalytic reactive sites [1,2,5–7]. Alloys forming a duplex scale consisting of an inner Cr_2O_3 phase and an outer $MnCr_2O_4$ phase have been developed in the last years and have shown promising results in decreasing chromium evaporation [2,5,8,9]. However, the oxidation rate, the electrical resistivity and the amount of the chromium in the outmost of the oxide scale on the interconnect alloys has still not been decreased enough for use in a commercial SOFC-stacks [1,5,9,10]. Application of coatings to improve the suitability of Crofer, and other chromia-forming alloys, has previously been demonstrated to be a promising route for further advancement [8,11–16]. Utilizing coatings has shown to decrease the oxidation rate of the alloys, and to decrease the electrical resistance of the formed oxides as well as to reduce the chromium evaporation and diffusion from the oxide surface [11,17–20]. To get a more detailed understanding of how coatings and steel interact, oxidation experiments of slurry coated Crofer 22APU were carried out. Coatings consisting of oxides belonging to different structure classes, fluorite, corundum, spinel and perovskite, and with very different chemical properties

* Corresponding author. Tel.: +45 21 32 54 93; fax: +45 4677 5858.
E-mail addresses: aase@risoe.dtu.dk (Å.H. Persson), larm@risoe.dtu.dk (L. Mikkelsen), pvhe@risoe.dtu.dk (P.V. Hendriksen), somers@mek.dtu.dk (M.A.J. Somers).
[1] Tel.: +45 4677 5811.
[2] Tel.: +45 4677 5725.

0925-8388/$ – see front matter © 2012 Elsevier B.V. All rights reserved.
doi:10.1016/j.jallcom.2011.12.095

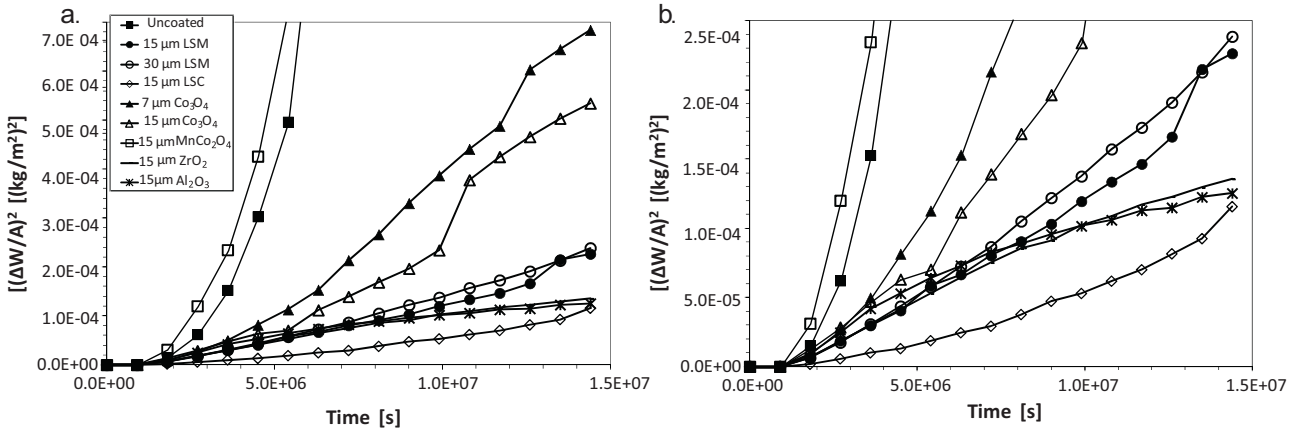

Fig. 1. The $(\Delta W/A)^2$–time plots for uncoated and coated Crofer 22APU samples in the long-term, cyclic oxidation experiment carried out at 900 °C in air containing 1% water vapour, (a) overview, (b) enlargement of (a) for relatively small weight increase, the key is the same for both plots.

were applied. The coatings included in the study were Al_2O_3, ZrO_2, $(La_{0.85}Sr_{0.15})_{1-x}Mn_{1+x}O_3 + (0.1-x)Mn_2O_3$ (referred to as LSM), $MnCo_2O_4$, 90 wt.% $(La_{0.85}Sr_{0.15})CoO_3$ + 10 wt.% Co_3O_4) (referred to as LSC), and Co_3O_4. None of the applied coatings contain Cr as one of the roles of the coating is to reduce the Cr activity on the surface of the coated steel to reduce the Cr evaporation rate. The chemical stability of the coating materials varies strongly over the series of materials (listed above in order of reducing stability). Whereas Al_2O_3 and ZrO_2 are extremely stable compounds (reduction pO_2 at 900 °C for $Al_2O_3 = 1.4 \times 10^{-39}$ atm and $ZrO_2 = 9.6 \times 10^{-40}$ atm [21]) the most unstable compounds used Co_3O_4 and LSC would decompose already during heating in air or under mild reduction (e.g. reduction pO_2 at 900 °C for CoO = 3.2×10^{-14} atm [21]), and hence very different interaction mechanisms between coating and steel could be anticipated over this series of materials. It should be noted that a technologically viable SOFC interconnect coating must provide good conductivity in the interface between interconnect and electrode. Whereas the four latter materials are good electronic conductors (e.g. $\sigma_{LSC} > 1000$ S/cm in air at 900 °C [22]) the two former (Al_2O_3 and ZrO_2) are poor electronic conductors (e.g. $\sigma_{Al_2O_3} < 10^{-7.5}$ S/cm in air at 1200 °C [23]). These materials are thus not directly applicable as single phase coatings in SOFC-stacks. The results allowed classifications of interaction mechanisms that can pave the road towards optimal coating designs.

2. Experimental

Crofer 22APU samples with the dimension 20 mm × 20 mm × 0.3 mm were etched for 30 min in a mixture of 75 vol.% H_2O + 5 vol.% HF + 20 vol.% HNO_3, to remove any native oxides formed during alloy processing. A series of samples was slurry coated on both sides using a hand held spray-gun, so that oxide thicknesses of approximately 7, 15 or 30 μm were applied. Simultaneously as the corrosion samples were sprayed a reference sample was sprayed, and the thickness of the applied coating on this reference sample was measured with a caliper. The coatings included in this study were ZrO_2, Al_2O_3, Co_3O_4, $MnCo_2O_4$, LSM, and LSC. The slurries consisted of approximately 33 wt.% powder of the coating material dissolved in ethanol with a small amount of polyvinyl pyrrolidone, (PVP)-binder. Before spraying onto the alloy substrates, the LSM, LSC, Co_3O_4 and $MnCo_2O_4$ slurries were ball-milled until a particle size of $Ø_{median}$ = 1–2 μm was achieved and the ZrO_2, Al_2O_3 slurry was ball-milled until a particle size of approximately $Ø_{median}$ = 3 μm was achieved.

The etched uncoated samples and the coated samples were weighed before mounting in the oxidation furnace with a volume of approximately 4.32×10^{-3} m^3. Air containing 1% water vapour was lead through the furnace with a flow rate of approximately 72×10^{-3} m^3/h. The samples were oxidized in 250-h cycles at 900 °C, after which they were weighed. The heating and cooling ramps were set to 120 °C/h. The total accumulated oxidation time was 4000 h. With a few exceptions, six samples of each corrosion sample type were prepared, corroded and removed from the furnace for further investigation after 500, 1000, 2000, and 4000 h of oxidation.

On one of the epoxy mounted Al_2O_3 coated samples, Focused Ion Beam (FIB) was used to prepare a Transmission Electron Microscope (TEM) sample for more detailed analysis of the alloy/oxide and oxide/coating interfaces and the oxide scale itself.

3. Results

3.1. Weight gain and microstructure

The weight gain data collected for the uncoated and coated Crofer samples during the cyclic oxidation experiment are presented as a weight increase^2–time plot in Fig. 1.

The plots of the uncoated Crofer sample and the Crofer samples coated with LSM, LSC, Co_3O_4, and $MnCo_2O_4$ are linear in Fig. 1 up to 1000 h oxidation, where break-away oxidation takes place for the uncoated and $MnCo_2O_4$ coated samples. The weight gain of the uncoated and $MnCo_2O_4$ coated samples was immense and since break-away oxidation was detected at an early stage the weight gain of these samples were ignored when zooming in on the weight gain of the rest of the samples in the study. Note, that the LSM, LSC, and Co_3O_4 coated samples continue to present linear behaviour up to 4000 h oxidation. The linearity in the weight increase^2–time plot indicates parabolic oxidation kinetics, as described by the expression in Eq. (1):

$$\Delta w^2 = k_p t_t + C, \quad (1)$$

Δw is the weight gain, while k_p and t_t are the parabolic rate constant and oxidation time, respectively. C is an integration constant correcting for transient oxidation, and here also for binder burn off from the coatings, which governs the initial weight measurements. Accordingly the first 250 h of oxidation is neglected. Parabolic oxidation indicates that the oxidation rate is determined by a diffusion process with constant diffusion coefficient resulting in a growth rate that decreases inversely proportionally to the oxide layer thickness [24].

The weight increase^2-time curves of the Al_2O_3 and ZrO_2 coated Crofer samples in Fig. 1 suggest deviations from parabolic oxidation, reflecting alternative reaction mechanisms in the system, i.e. the protective action of the scale effectively increases over time. The weight gain curves of the Al_2O_3 and ZrO_2 coated samples are deflected downwards, while the weight gain curves of all the other samples in this study are either linear or deflecting ever so slightly upwards.

Apart from $MnCo_2O_4$ all the coatings lowered the weight gain compared to the uncoated Crofer 22APU. The parabolic oxidation constants for the uncoated and the coated Crofer 22APU samples are summarized in Tables 1a and 1b. For the Co_3O_4 coated sample a slight increase in the parabolic oxidation constant was observed

Table 1a
Parabolic rate constants for the coated and uncoated Crofer samples estimated from the 4000 h oxidation, the weight gain from the first 250 h is neglected.

	k_p [kg^2 m^{-4} s^{-1}]	Time [h]	Remark
15 μm LSC	$(0.6 \pm 0.2) \times 10^{-11}$	4000	
15 μm Al_2O_3	$(1.6 \pm 0.08) \times 10^{-11}$	1000	Deviation from parabolic ox.
	$(0.9 \pm 0.2) \times 10^{-11}$	1000–4000	
15 μm ZrO_2	$(1.1 \pm 0.09) \times 10^{-11}$	1500	Deviation from parabolic ox.
	$(0.9 \pm 0.07) \times 10^{-11}$	1500–4000	
15 μm LSM	$(1.4 \pm 0.2) \times 10^{-11}$	4000	
30 μm LSM	$(1.4 \pm 0.2) \times 10^{-11}$	4000	
15 μm Co_3O_4	$(1.7 \pm 0.6) \times 10^{-11}$	2750	
	4.4×10^{-11}	3000–4000	
7 μm Co_3O_4	$(3.6 \pm 1.2) \times 10^{-11}$	4000	
15 μm $MnCo_2O_4$	$(9.4 \pm 1.5) \times 10^{-11}$	1250	
Uncoated	$(8.2 \pm 2.5) \times 10^{-11}$	1000	

during the last 1000 h of oxidation. For the Al_2O_3 and ZrO_2 coated samples a significantly lower parabolic oxidation constant was observed after 1000 h of oxidation.

Also included in Tables 1a and 1b are the thicknesses of the formed oxide scales on the oxidized samples as determined from the SEM micrographs of the sample cross-sections. Figs. 2–4 show examples of such cross-sections for the samples oxidized for 500, 1000, 2000, and 4000 h. The thickness of the scale varies over the interface as indicated by the standard deviation, deduced from measuring the scale thickness at ~40–60 different positions, also included in the table. The samples are ordered in Tables 1a and 1b according to their total weight gain observed, i.e. the protective action of the coating decreases as one moves down in the table.

The duplex character of the oxide scale on uncoated Crofer [8,25] is visible in the micrographs in Fig. 2, where the outer (Mn,Cr)-spinel phase is lighter grey than the inner Cr_2O_3 phase. Metallic inclusions (light) are observed in the oxide scale as well as internal oxides (black) in the metallic bulk just under the oxide scale. The internal oxides consist of TiO_2 and Al_2O_3 and are observed on all the coated samples [8].

In the case of the Al_2O_3 and ZrO_2 coated samples the coating particles are incorporated into the growing oxide scale (Fig. 2). The black Al_2O_3 particles are easier to identify in the growing oxide scale due to their size, and maybe also due to their larger tendency to become incorporated.

In the growing oxide scale on the LSC coated samples, bright La- and Sr-rich particles appear to be incorporated. These areas probably consist of $LaCrO_3$ and/or $SrCrO_4$ and are formed by a reaction between chromium and the coating. The LSC coated samples also present a thinner oxide scale than the uncoated samples, but the oxide/alloy and oxide/coating interfaces are not as smooth and well defined as on the LSM coated samples. The micrographs of the LSM coated samples in Fig. 3 show a thinner oxide scale and fewer metal inclusions than on the uncoated samples. The heavier, bright LSM particles appear to be pushed ahead of the outwardly growing oxide scale and are not incorporated into the oxide scale.

The oxide scale on the Co_3O_4 coated samples consists of a Cr_2O_3 layer (darker layer on the SEM images), and a spinel phase layer (the lighter grey layer) (Figs. 3 and 4). The thicknesses of both layers are specified in Table 1b for both the 7 μm and 15 μm Co_3O_4 coated samples. The spinel phase layer consists of the sintered/reacted Co_3O_4 coating.

The micrographs of the $MnCo_2O_4$ coated samples in Fig. 4 show a similar subdivision in a Cr_2O_3 layer and a spinel phase as found on the Co_3O_4 coated samples. After approximately 1000 h of oxidation the edges of the $MnCo_2O_4$ coated samples started to experience accelerated oxidation. This was not observed on any of the other coated samples, where the oxide scales on the edges appeared similar to the oxide found along the flat surfaces of the samples. The uncoated samples had some heavy oxidation on the edges as well, as illustrated in the micrograph of an uncoated sample oxidized for 3000 h in Fig. 2. The $MnCo_2O_4$ coated samples also showed the thickest oxide scale of all oxidized samples (Table 1b).

3.2. Composition analysis with EDS

The amount of Cr in the outer part of the formed, dense oxide scale was determined with point analysis (Table 2). The "outer part" is effectively the outer 2 μm of the dense part of the oxide layer (Figs. 2–4).

For the Co_3O_4 coated samples the outer oxide scale corresponds to the outer part of the sintered/reacted coating as indicated in Fig. 4. This means that any Cr detected in the outer oxide scale on the spinel coated samples must have diffused through both the forming oxide scale and the sintered/reacted spinel coating thereby a longer distance compared to the uncoated samples and in the LSM, LSC, Al_2O_3 and ZrO_2 coated samples. The chromium content is accordingly observed to be lower (Table 2). The cation compositions found in the outer oxide scale on all samples fall within a spinel phase region according to the Cr—Co—Mn phase diagram in Fig. 5. The calculated spinel compositions are listed in Table 2. The spinel compositions found in the outer oxide scales on the oxidized samples are determined by the diffusion rates of the various cations; in the mono-phase cubic spinel in the Co—Mn—Cr—O system which has a broad homogeneity range at 900 °C (cf. Fig. 5).

As shown in Table 2 a composition close to $MnCr_2O_4$ is observed on the uncoated Crofer samples as expected [8,25]. The composition of the outer oxide scale for ZrO_2 coated samples is the same as the spinel found on uncoated samples. For the Al_2O_3 coated samples a

Table 1b
Measured oxide scale thicknesses, *t*, on the BSE micrographs.

	t [μm] 500 h	*t* [μm] 1000 h	*t* [μm] 2000 h	*t* [μm] 4000 h	Remark
15 μm LSC	4.1 ± 1.2	4.3 ± 1.6	5.4 ± 1.5	9.2 ± 1.9	Tot. ox. scale[a]
15 μm Al_2O_3			10.0 ± 1.5	8.5 ± 2.4	Tot. ox. scale[a]
15 μm ZrO_2		8.3 ± 1.7	9.8 ± 1.8	11.8 ± 2.3	Tot. ox. scale[a]
15 μm LSM	4.7 ± 1.6	6.5 ± 1.7	7.3 ± 1.3	10.6 ± 2.8	Tot. ox. scale[a]
15 μm Co_3O_4	5.6 ± 1.6 (10.6 ± 2.0)	6.8 ± 2.0 (13.3 ± 3.8)	9.2 ± 1.9 (16.2 ± 2.8)	14.5 ± 1.8 (21.0 ± 2.7)	Cr_2O_3 scale (Formed oxide + sintered/reacted coating)[b]
7 μm Co_3O_4	7.1 ± 1.4 (10.5 ± 2.0)	8.4 ± 1.7 (10.3 ± 1.8)	15.2 ± 3.0 (19.2 ± 7.0)	14.9 ± 4.0 (16.6 ± 4.5)	Cr_2O_3 scale (Formed oxide + sintered/reacted coating)[b]
15 μm $MnCo_2O_4$	8.5 ± 1.0 (15.5 ± 1.4)	13.3 ± 1.5 (21.2 ± 3.1)	19.1 ± 1.8 (26.4 ± 2.7)	25.±3.0 (31.6 ± 3.2)	Cr_2O_3 scale (Formed oxide + sintered/reacted coating)[b]
Uncoated	9.8 ± 3.2	11.9 ± 2.9	15.3 ± 2.0		Tot. ox. scale[a]

[a] Tot. Ox. Scale = Total Newly formed Oxide Scale.
[b] Formed oxide + sintered/reacted coating = Newly formed oxide + the sintered/reacted coating.

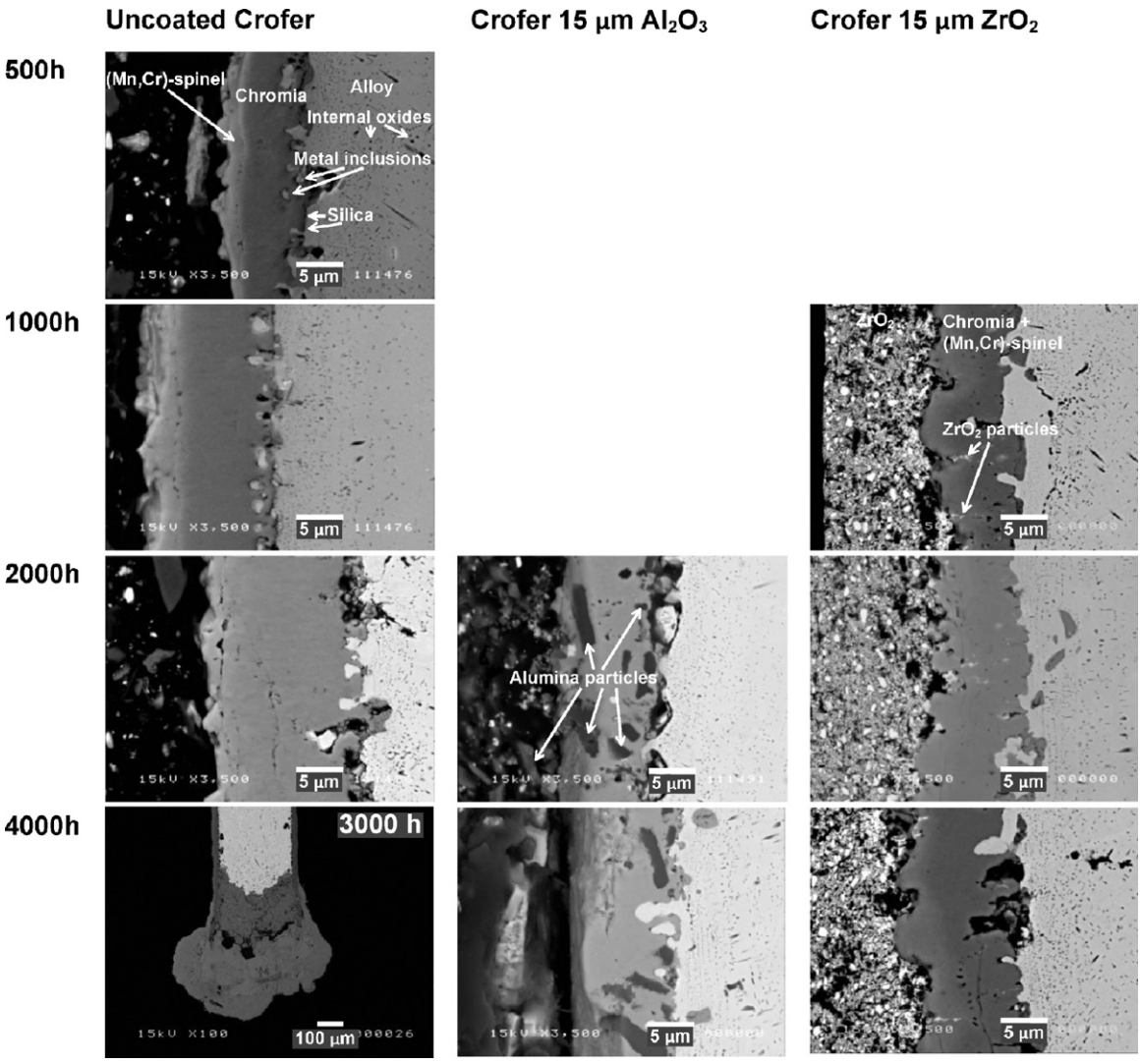

Fig. 2. BSE micrographs of the oxide scales in the cross-sections of the samples, with the oxidation times indicated left of the pictures, note though that the oxidized uncoated sample in the down left corner only was oxidized for 3000 h.

spinel with about 40/60 Mn- and Cr-content is found with a slight addition of Al after 2000 and 4000 h oxidation. The presence of a LSC coating reduces the Cr-content, while the Co-content is increased. The presence of a LSM coating reduces the Cr content in the outer spinel in favour for Mn in comparison to the spinel composition found on uncoated Crofer samples. This has also been observed in previous oxidation studies [26]. When studying the spinel composition in the outer oxide scale for the Co_3O_4 coated samples, it is found that the samples with the thicker coating have a significantly lower Mn content as compared to the thinner coating and also a slightly lower Cr-content. The Cr-content in the outer oxide scale for the $MnCo_2O_4$ coated samples is the lowest of all samples in Table 2.

EDS-mappings were made on the oxide scales to get an overview of the composition of the scales. On these mappings the relative areas of the spinel and chromia phases can be measured. The results are presented in Table 3.

The results in Table 3 clearly show that the presence of a coating increases the spinel ratio of the scale. The Co_3O_4 and $MnCo_2O_4$ coated samples show high spinel ratios, at least initially. However, it should be noted that the spinel phase on these samples consists of both sintered/reacted spinel coating and the forming spinel phase during the oxidation process. As seen from the SEM micrographs in Figs. 3 and 4 it is impossible to visually discriminate among the two spinels.

4. Discussion

The observations and the effect of the six different coatings are discussed and compared to the oxidation behaviour of the uncoated sample and each other, in the order of:

Uncoated
Al_2O_3
ZrO_2
LSC
LSM
Co_3O_4
$MnCo_2O_4$

Based on the observations three main types of interaction mechanisms between the coatings and the forming oxides during oxidation could be formulated:

(A) Incorporation of coating particles in the growing oxide scale
(B.1) Coatings that sinter/react with the growing oxide scale

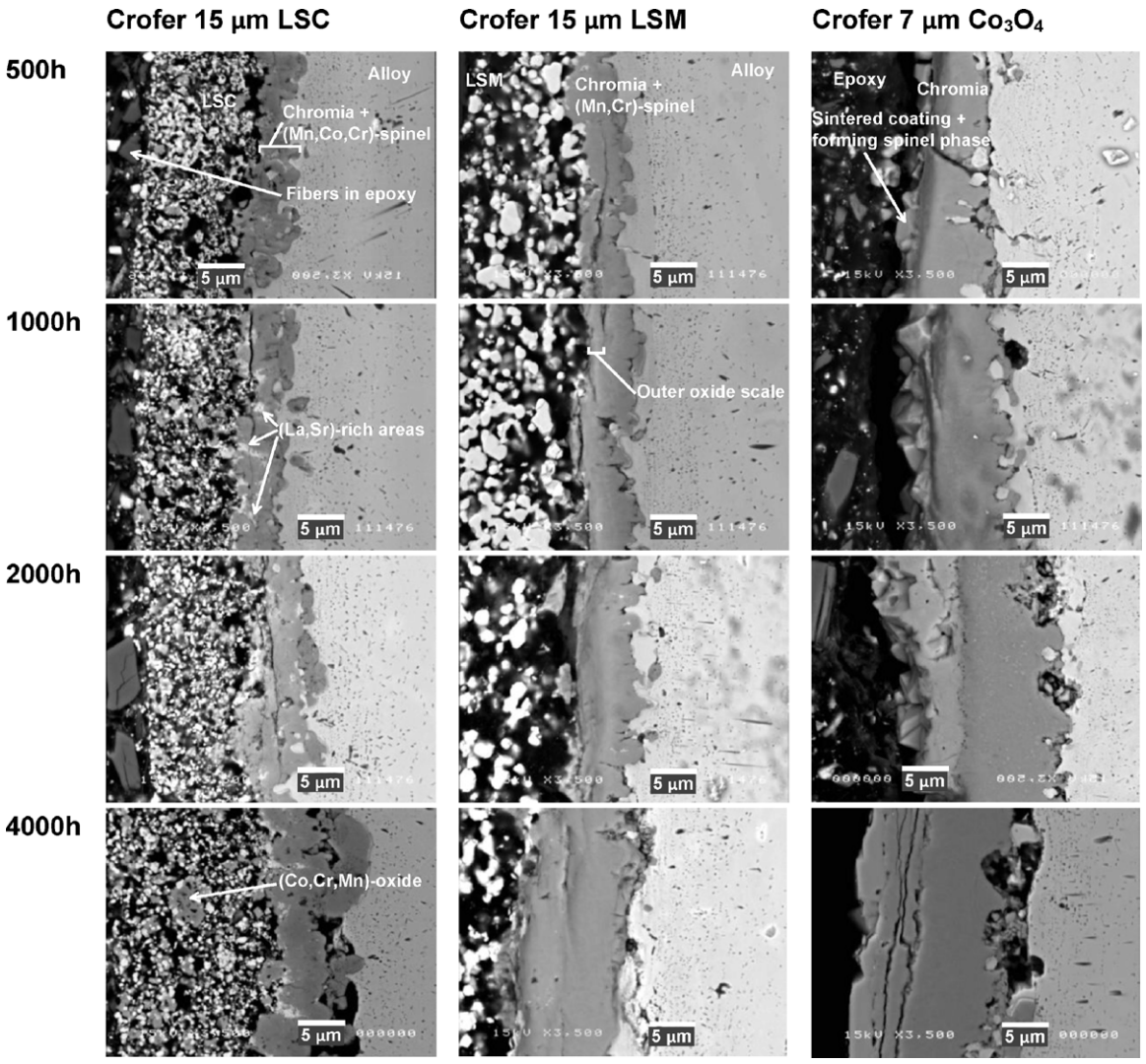

Fig. 3. BSE micrographs of the oxide scales in the cross-sections of the samples, with the oxidation times indicated left of the pictures.

(B.2) Partial incorporation of the coating that reacts with the growing oxide scale, while main part of the coating remains porous

(C) Elemental addition into the growing oxide scale from a coating that remains porous and is pushed in front of the growing oxide scale

4.1. Uncoated samples

In Fig. 6a. the diffusive fluxes during the oxidation and oxide layer growth of uncoated Crofer are drawn schematically.

According to literature, the chromia scale on chromia-forming alloys grows through counter diffusion of Cr-cations and O-anions with formation of chromia within the chromia scale[24]. Accordingly local growth stresses develop [24]. It has been shown that the outward diffusion of Cr-cations is the dominating diffusion flux during chromia formation, i.e. the faster of the two diffusing species. This means that the oxide phase growth occurs close to the chromia/spinel interface, i.e. interface **II**.

A wavy oxide–alloy interface is observed with metallic protrusions and inclusions in the oxide. This may be explained by compressive stresses within the alloy as a result of internal oxidation [27]. Another explanation for the convoluted interface may be the formation of compressive growth stresses in the oxide scale [28]. The oxygen lattice in a spinel is presumed to be fully occupied, and no significant inward oxygen diffusion takes place [29]. Crofer naturally forms a duplex oxide scale consisting of a (Mn,Cr)-spinel on top of a chromia layer [30]. The effect of this outer spinel phase is a drop of the oxygen potential in local equilibrium within the chromia layer, and thereby lowering of the inward diffusion of oxygen ion through the chromia phase. The presence of the outer spinel layer on uncoated Crofer therefore shifts the growth of the chromia scale further towards the chromia/spinel interface. The presence of inclusions in uncoated Crofer may be partly caused by inward anion diffusion in the Cr_2O_3 phase, as discussed above. The presence and growth of (Cr, Mn)-spinel on uncoated samples can be explained by diffusion of Mn species through the chromia layer as indicated in the diffusion model in Fig. 6a. Mn-diffusion through Cr_2O_3 proceeds faster than Cr-diffusion [31]. Possible interface reactions at the chromia/alloy interface, interface **I**, are listed as reactions **Ia** and **Ib** in Table 4 The outward diffusing Cr^{3+} and $Mn^{2+/3+}$ ions are probably diffusing via interstitials along the grain boundaries in the chromia phase [31–33]. These outward diffusing cations consume oxygen from the spinel phase to form chromia at the chromia/spinel interface, interface **II**, or incorporate oxygen that diffuses into the chromia layer.

The spinel phase is exposed to atmospheric pressure, which suggests that the available point defects for cation diffusion in the spinel phase are cation vacancies [34–39]. These vacancies, created at the spinel surface during oxygen uptake, diffuse inward corresponding to an outward diffusive flux of Cr- and Mn-ions. In

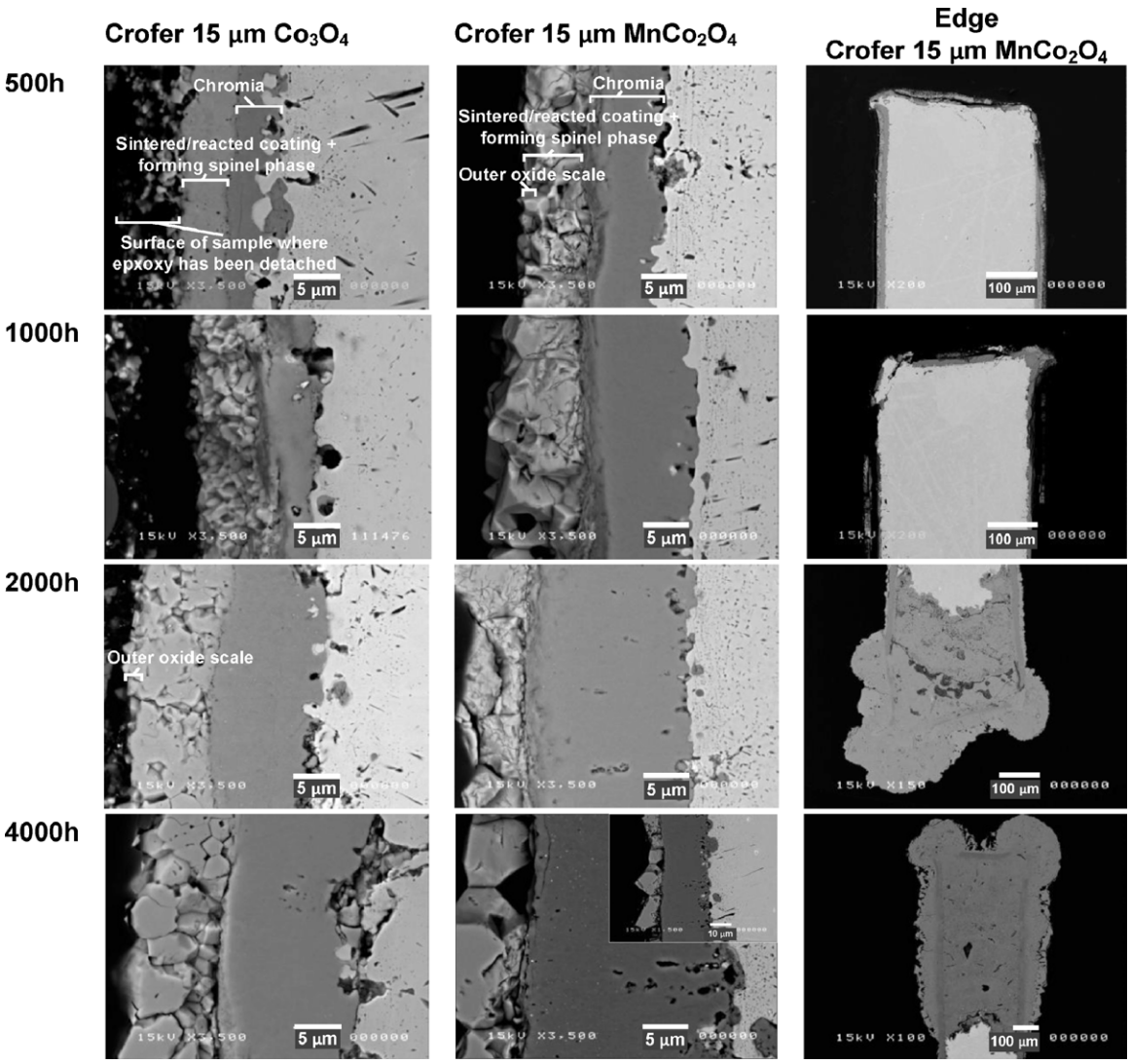

Fig. 4. BSE micrographs of the oxide scales in the cross-sections of the samples, with the oxidation times indicated left of the pictures.

interface reaction **IIIa** in Table 4, an interface reaction describing oxygen uptake at the spinel/atmosphere interface, interface **III**, is suggested. The morphology of the scale on the uncoated samples in Fig. 2 supports the hypothesis that the oxide scale grows mainly by outward cation diffusion. The presence of SiO_2 filled coalesced Kirkendall voids at the alloy/chromia interface [40] and Kirkendall voids at the chromia/spinel interface are consistent with dominant outward cation diffusion.

Interface reactions describing all these situations are listed in Table 4. These reactions show that when chromia is formed in interface **II** according to interface reaction **IIa** four unit cells of chromia, $\Delta(B)$, are formed at the expense of three unit cells of spinel, $\Delta(C)$. At the same time it is observed that when spinel is formed in interface **II** according to interface reaction **IIb** three unit cells of spinel, $\Delta(C)$, are formed at the expense of four unit cells of chromia, $\Delta(B)$. A second possible interface reaction where spinel can form in interface **II** is listed in interface reaction **IIc.** This interface reaction does not result in any changes in the number of unit cells.

4.2. Al_2O_3 coating

In the micrograph in Fig. 2 incorporation of the Al_2O_3 coating particles was observed in both the chromia and the spinel phase of the oxide scale. Provided that Al_2O_3 particles continue

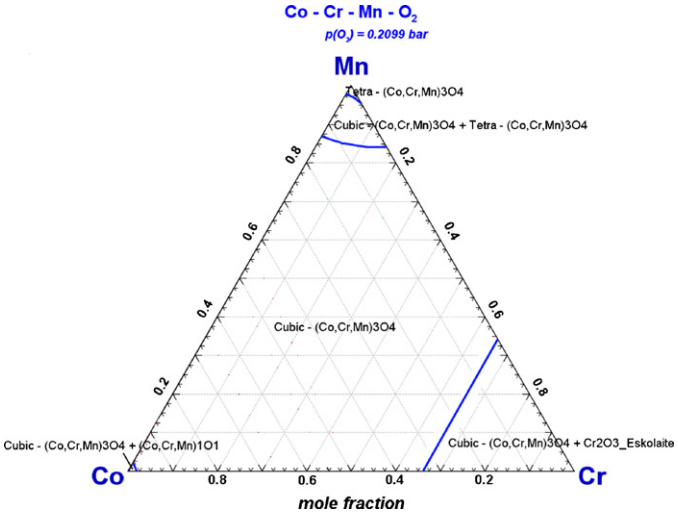

Fig. 5. Co—Mn—Cr—O phase diagram at 900 °C [21].

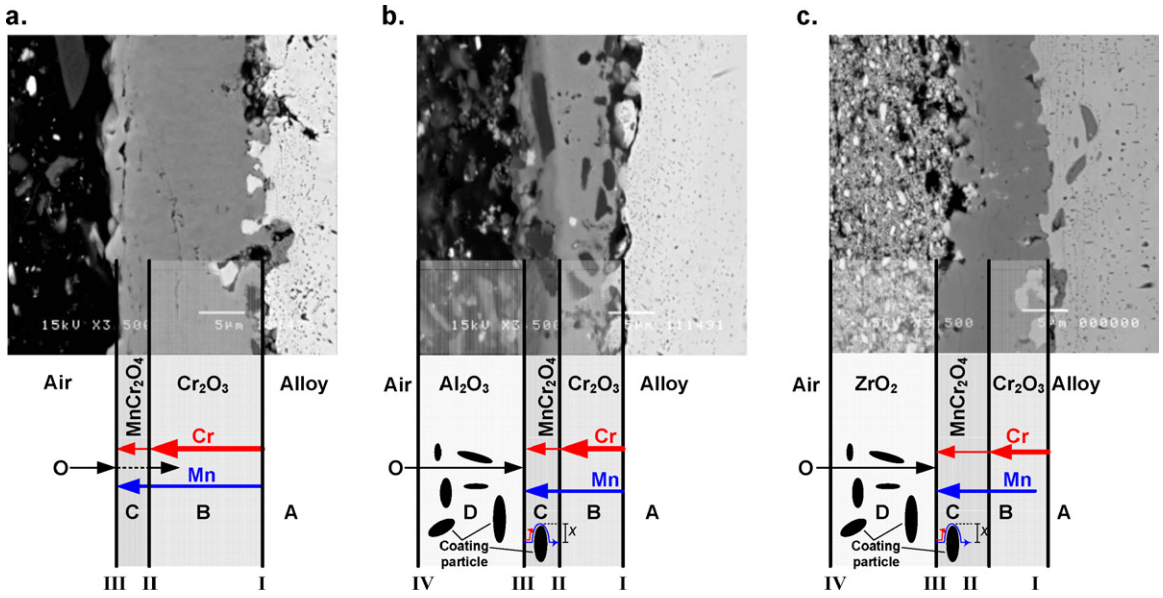

Fig. 6. Diffusion model of ions during oxidation of (a) uncoated Crofer, (b) Al_2O_3 coated Crofer, and (c) ZrO_2 coated Crofer on micrographs of samples oxidized for 2000 h.

to become incorporated into the growing oxide scale, these particles will give a continuous geometrical protection against oxidation throughout the oxidation process, since the outward diffusing Mn- and Cr-cations are forced to diffuse an extra distance, *x*, around the incorporated coating particles to reach the oxide surface, as illustrated in Fig. 6b. As the oxide scale grows thicker, more coating particles will become incorporated, and the extra diffusion distance, implemented by their presence, will be of the same magnitude as the thickness of the oxide scale.

Al_2O_3 is thermodynamically relatively stable, but aluminium can be dissolved in both $MnCr_2O_4$ and Cr_2O_3 when the Al_2O_3 coating particles are incorporated into the growing oxide scale, albeit the kinetics are slow. The aluminium signals detected in the outer spinel phase on the forming oxide scale in Table 2 could originate from this dissolved aluminium, but most likely originates from Al_2O_3 coating particles embedded in the oxide scale not visible on the micrographs. The (Mn,Cr)-spinel composition remaining if the aluminium signal is ignored is similar to the spinel composition formed on uncoated Crofer samples, only with a slightly higher Mn content. The EDS mapping in Fig. 7b. shows that an extra amount of Mn is found in close vicinity of the alumina particles. The original micrograph is presented in Fig. 7a. This can be explained by a relatively slow Cr diffusion on Al_2O_3 particles [6], suggesting that the faster diffusing manganese probably is diffusing around the Al_2O_3 coating particles faster than chromium, forming a more Mn-rich oxide phase. The Al_2O_3 coating leads to increase of the spinel ratio to approximately 30% compared to 10% for the uncoated Crofer samples after 2000 h oxidation.

The pale orange area in the EDS map symbolises a Mn containing spinel phase. This phase is found on top of the chromia phase. However, the spinel phase is also found closer to the alloy/oxide interface on the outer side of the large Al_2O_3 coating particle incorporated in the oxide scale. The micrographs and EDS mapping in Fig. 7 is only one example of this phenomenon that was observed at several places on the polished cross-section of the oxidized Al_2O_3 coated sample. Detailed analyses of feasible reactions between Al_2O_3 and Cr_2O_3 or $MnCr_2O_4$ as well as the composition around the Al_2O_3 particles were investigated by preparing a TEM sample

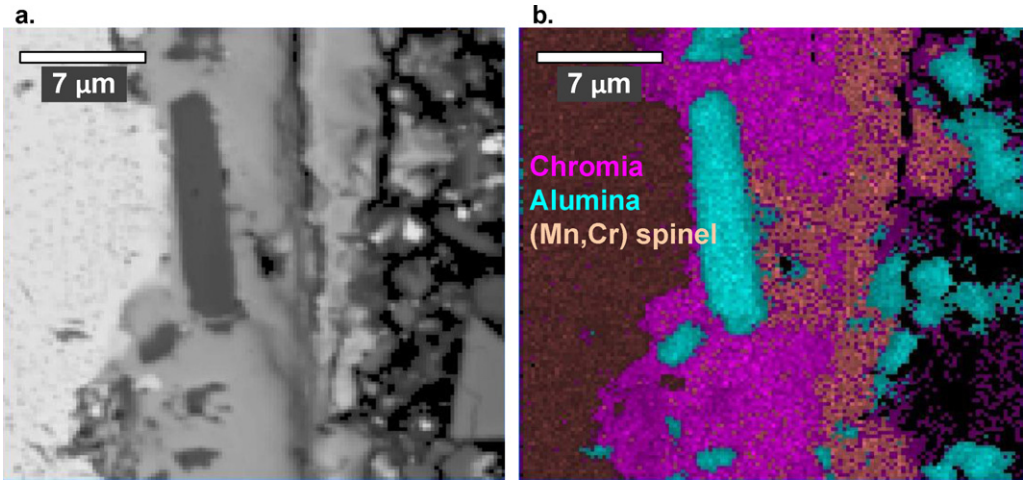

Fig. 7. Mapping of the alumina coated sample oxidized for 2000 h (for interpretation of the references to color in this figure legend, the reader is referred to the web version of the article).

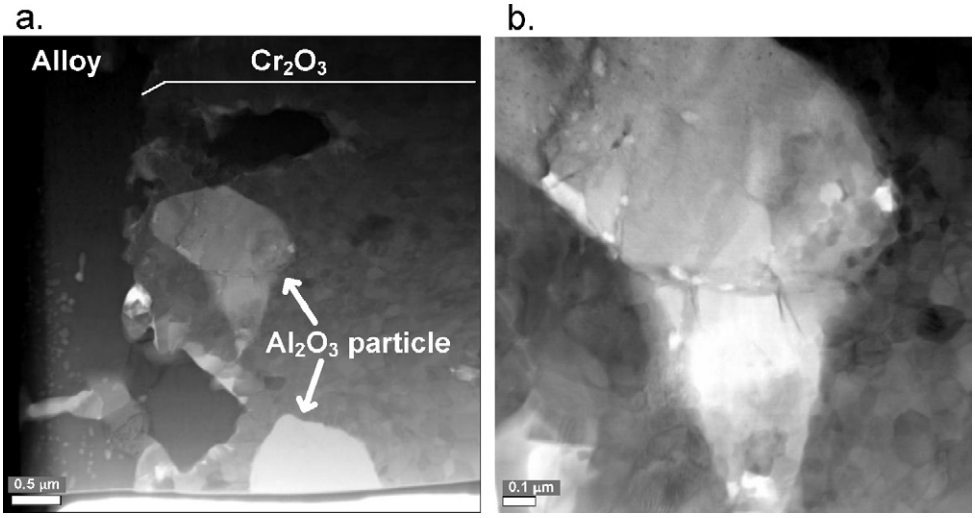

Fig. 8. TEM micrographs of polished cross-section of Al_2O_3 coated Crofer sample oxidized for 2000 h in air containing 1% water, (a) overview of interface II and (b) enlargement of alumina particle in (a).

by FIB. A TEM micrograph of an embedded Al_2O_3-particle is visible in Fig. 8. The analyses of the oxide composition on all sides of the Al_2O_3-particle indicate Cr_2O_3 and only few traces of Mn and Al. No Mn and only minor traces of Cr were detected inside the Al_2O_3-particle. The alumina particle in this micrograph is smaller than the one illustrated in Fig. 7. Since the particle is smaller the chromium ions have been able to completely incorporate it in a chromia phase in contrast with the larger particle in Fig. 7. Considering the grains in the chromia layer in the oxide scale it is also possible to discern that the chromia grains specifically around the alumina particle are smaller than further away from the alumina particle (Fig. 8b).

Deviation from parabolic oxidation behaviour was observed for the Al_2O_3 coated sample (cf. Fig. 1). During ideal parabolic oxidation the oxidation rate decreases with time due to the oxide scale growing thicker, thus creating longer diffusion distance for the ions [24]. On the Al_2O_3 coated samples the above described and discussed extensive incorporation of coating particles introduces even longer diffusion distances for the ions as the scale grows (scale thickness + x), thus resulting in the scale becoming more and more protective as it grows, which could lead to the observed deviation from parabolic growth for long times.

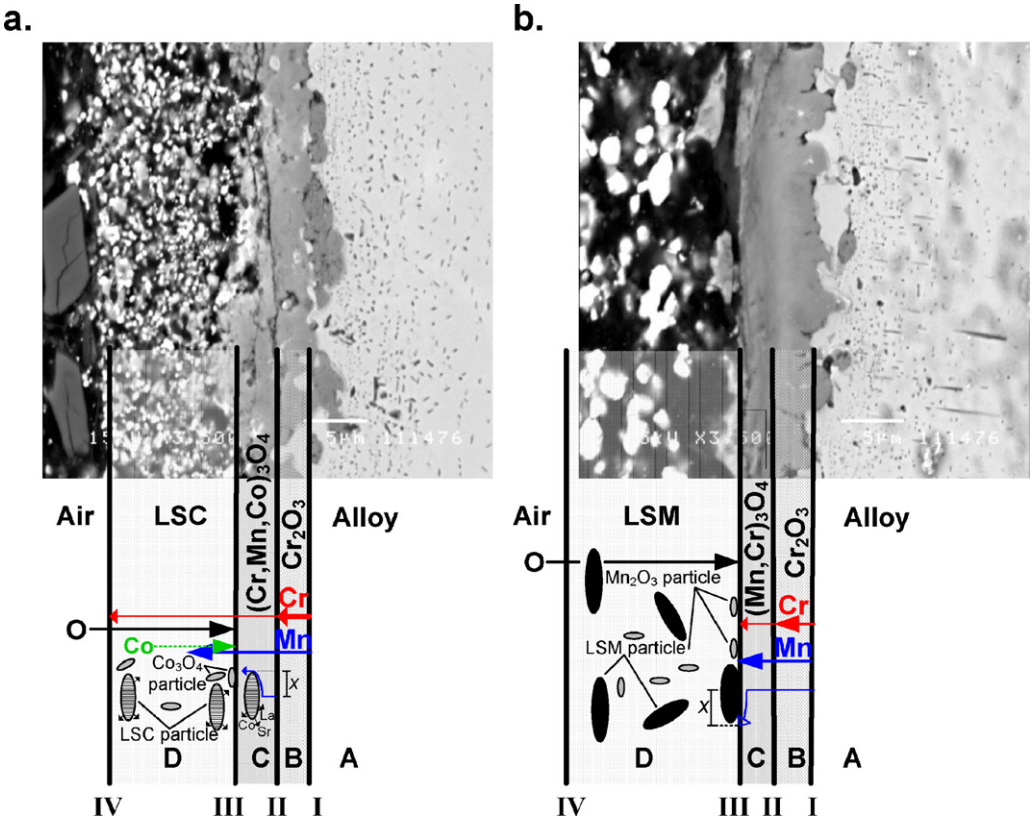

Fig. 9. Diffusive fluxes during oxidation of (a) LSC coated Crofer and (b) LSM coated Crofer on micrographs of samples oxidized for 2000 h.

Table 2
Cation content in the formed spinel (of the general formula M_3O_4) in the outer oxide scale on the uncoated and coated Crofer samples oxidized in the long-term cycling oxidation experiment at 900 °C in air containing 1% water.

	500 h				1000 h				2000 h				4000 h			
	Cr	Mn	Co	Fe	Cr	Mn	Co	Fe	Cr	Mn	Co	Fe	Cr	Mn	Co	Fe
Uncoated	1.9 ± 0.1	1.1 ± 0.1			1.6 ± 0.2	1.4 ± 0.2			1.7 ± 0.3	1.2 ± 0.4		0.1 ± 0.0				
15 μm ZrO_2					1.8 ± 0.1	1.1 ± 0.1			1.9 ± 0.3	1.0 ± 0.3			1.9 ± 0.1	1.0 ± 0.1		
15 μm LSC	1.4 ± 0.5	0.6 ± 0.3	0.9 ± 0.2	0.1 ± 0.0	1.5 ± 0.4	0.5 ± 0.2	0.9 ± 0.2	0.1 ± 0.1	1.3 ± 0.4	0.7 ± 0.4	0.9 ± 0.1	0.1 ± 0.1	1.6 ± 0.3	0.5 ± 0.2	0.8 ± 0.1	0.1 ± 0.1
15 μm LSM	1.4 ± 0.1	1.5 ± 0.1			1.5 ± 0.2	1.4 ± 0.2			1.6 ± 0.2	1.3 ± 0.2			1.6 ± 0.1	1.3 ± 0.1		
7 μm Co_3O_4	0.3 ± 0.0	1.2 ± 0.2	1.1 ± 0.1	0.4 ± 0.1	0.7 ± 0.1	1.3 ± 0.2	0.9 ± 0.3	0.1 ± 0.0	0.6 ± 0.2	1.2 ± 0.3	1.0 ± 0.2	0.2 ± 0.1	0.8 ± 0.1	1.4 ± 0.1	0.7 ± 0.2	0.2 ± 0.1
15 μm Co_3O_4	0.6 ± 0.1	0.2 ± 0.1	2.1 ± 0.1		0.6 ± 0.1	0.4 ± 0.1	2.0 ± 0.1		0.4 ± 0.1	0.3 ± 0.2	2.2 ± 0.2		0.7 ± 0.3	0.4 ± 0.2	1.9 ± 0.2	0.1 ± 0.0
15 μm $MnCo_2O_4$	0.1 ± 0.0	1.2 ± 0.1	1.6 ± 0.2		0.1 ± 0.0	1.3 ± 0.2	1.6 ± 0.2		0.2 ± 0.1	1.3 ± 0.2	1.4 ± 0.2	0.1 ± 0.1	0.5 ± 0.1	1.1 ± 0.1	1.3 ± 0.1	0.1 ± 0.0
									1.4 ± 0.3	1.1 ± 0.3	0.4 ± 0.4	0.1 ± 0.0	1.6 ± 0.3	0.9 ± 0.2	0.4 ± 0.2	0.1 ± 0.0

Table 3
Spinel ratio (area of spinel phase/total area of oxide scale) of the total oxide scale on uncoated and coated Crofer samples oxidized at 900 °C in air containing 1% water.

	500 h	1000 h	2000 h	4000 h
Uncoated	0.15	0.09	0.10	
15 μm Al_2O_3			0.36	<0.20
15 μm ZrO_2		0.40	0.30	0.32
15 μm LSC	0.49	0.44	0.40	0.41
15 μm LSM	0.41	0.35	0.43	0.39
7 μm Co_3O_4	0.33	0.34	0.26	0.09
15 μm Co_3O_4	0.53	0.53	0.47	0.34
15 μm $MnCo_2O_4$	0.51	0.39	0.30	0.30

4.3. ZrO_2 coating

As displayed in Fig. 1 the ZrO_2 coated samples showed similar deviation from parabolic oxidation behaviour as the Al_2O_3 coated samples. Just as the Al_2O_3 coating the ZrO_2 coating decreases the oxidation rate of the Crofer 22APU samples compared to the uncoated samples. The micrographs in Fig. 2 show tendencies of the incorporation of bright ZrO_2 particles in the outer part of the growing oxide scale. The performed point analyses of the outer oxide scale presented in Table 2 show a spinel composition similar to the spinel composition found on uncoated samples. The ZrO_2 coating does not affect the oxide composition; instead it functions simply as a geometrical protection against oxidation. The possible diffusive fluxes during oxidation are presented in Fig. 6c.

Just as the Al_2O_3 coating the ZrO_2 coating remains porous throughout the oxidation experiment, as can be seen in the micrographs in Fig. 2. The interface reactions on the ZrO_2 coated samples are assumed to be similar to the ones for uncoated Crofer listed in Table 4.

The ZrO_2 coating particles do not affect the chemical composition of the forming oxide, but it does appear to affect the spinel ratio of the oxide scale. In comparison to the uncoated samples the ratio has increased from 10% to 30–40%. Like for the alumina particles the ZrO_2 particles seem to block for the Cr-ions more efficiently than for the Mn-ions [6,31], leading to an increase of the spinel ratio. The incorporated ZrO_2 particles do not dissociate and do not react with the surrounding Cr_2O_3 and $MnCr_2O_4$ oxide scale, since ZrO_2 is thermodynamically more stable, which agrees with the observation of an unchanged spinel composition in the oxide compared to the uncoated sample. All these effects were also listed for the Al_2O_3 coated samples. The impact of these effects is apparently larger for the Al_2O_3 coated samples than for the ZrO_2 coated

Table 4
Possible interface reactions on uncoated Crofer with the changes in number of unit cells in the chromia and spinel phase, $\Delta(B/C)$, where B and C refer to chromia and spinel phase, respectively.

Interface	Reaction equation	$\Delta(B)$	$\Delta(C)$
Uncoated Crofer			
Ia	$Cr \rightarrow (Cr_I^{\bullet\bullet\bullet} + 3e')_B$	0	
Ib	$Mn \rightarrow (Mn_I^{\bullet\bullet} + 2e')_B$	0	
IIa	$8(Cr_I^{\bullet\bullet\bullet} + 3e')_B + 3(2V_M''' + V_M'' + 4O_O^x + 8h^\bullet)_C \rightarrow 4Cr_2O_3$	4	−3
IIb	$4Cr_2O_3 + 4(Mn_I^{\bullet\bullet} + 2e')_B + (2V_M''' + V_M'' + 4O_O^x + 8h^\bullet)_C \rightarrow 4MnCr_2O_4$	−4	3
IIc	$2(Cr_I^{\bullet\bullet\bullet} + 3e')_B + (Mn_I^{\bullet\bullet} + 2e')_B + (2V_M''' + V_M'' + 4O_O^x + 8h^\bullet)_C \rightarrow MnCr_2O_4$	0	0
IIIa	$6O_2 \rightarrow 3(2V_M''' + V_M'' + 4O_O^x + 8h^\bullet)_C$		3
Co containing spinel on coated Crofer			
IId	$12Cr_2O_3 + 8Cr_{0.6}Mn_{1.2}Co_{1.2}O_4 \rightarrow 16Cr_{1.8}Mn_{0.6}Co_{0.6}O_4 + (2V_{Cr}''' + V_{Mn}'' + 4O_O^x + 8h^\bullet)$	−4	3

Table 5
The extra interface reaction at interface **III** on LSC and LSM coated Crofer and the ΔG of the reactions at 900 °C in air calculated by FactSage 5.5 [21].

Interface	Reaction equation	ΔG [kJ]
LSC coated Crofer		
IIIc	$40(La_{0.85}Sr_{0.15})CoO_3 + 40MnCr_2O_4 + 3O_2(0.21\ atm) \rightarrow 34LaCrO_3 + 6SrCrO_4 + 40CrMnCoO_4$	−1826.4
LSM coated Crofer		
IIIb	$6(Mn_2O_3)_D + 12(MnCr_2O_4)_C \rightarrow 16(Mn_{1.5}Cr_{1.5}O_4)_C + O_2(0.21\ atm)$	−163.8
IIId	$40(La_{0.85}Sr_{0.15})MnO_3 + 40MnCr_2O_4 + 3O_2(0.21\ atm) \rightarrow 34LaCrO_3 + 6SrCrO_4 + 40CrMn_2O_4$	436.3

samples. Differences in the particle sizes of the Al_2O_3 and ZrO_2 coatings (the Al_2O_3 coating has larger particle size) might explain the larger deviation from parabolic oxidation behaviour for Al_2O_3 coated samples.

4.4. LSC coating

Via applying a LSC coating on the surface of Crofer 22APU samples the oxidation rate was decreased significantly. The LSC coating remains porous during oxidation and does not provide any hindrance for oxygen to reach the surface. In Fig. 9a, the diffusive fluxes are illustrated.

The interface reactions are assumed to be similar to the ones listed for uncoated Crofer in Table 4, but a fourth interface reaction in interface **II** could be possible when the cobalt containing spinel phase reacts with chromia. Reaction **IId** in Table 4 is a suggested example of such a reaction.

The $(La_{0.85}Sr_{0.15})CoO_3$ perovskite is thermodynamically stable at the oxidation conditions; however, under the interaction with Mn- and Cr-ions from the FeCr-alloy it partly dissociates into $LaCrO_3$, $SrCrO_4$ and (Co,Cr,Mn)-spinel. The $LaCrO_3$ and $SrCrO_4$ containing areas are easily spotted as small bright particles within the oxide scale, mainly in the spinel layer. A possible interface reaction accounting for the decomposition of the LSC at the interface between spinel and coating, interface **III**, is listed in Table 5 together with the Gibbs free energy change for the reaction [21].

The incorporated $SrCrO_4$ and $LaCrO_3$ particles provide a geometrical protection against oxidation, just as the incorporated Al_2O_3 and ZrO_2 particles on the Al_2O_3 and ZrO_2 coated samples. The effect is illustrated in Fig. 9a.

It should however be emphasized that there is no complete reduction reaction of the LSC coating. The outer part of the LSC coating remains a $(La_{0.85}Sr_{0.15})CoO_3$ perovskite, and as seen in the micrographs in Fig. 3 the LSC coating remains porous throughout oxidation, even though small areas of $(Co,Cr,Mn)_3O_4$ oxides form out in the LSC coating when the outwardly diffusing Mn- and Cr-ions originating from the alloy react with the spinel oxides in the coating (Fig. 3).

4.5. LSM coating

The LSM coating is, as can be observed in the micrographs in Fig. 3, porous. An estimation of the porosity of the LSM coating based on the micrographs gives a value of approximately 30–40% with pore sizes of approximately 1 μm. This shows that during oxidation unlimited access to oxygen is to be expected at the surface of the forming oxide scale. A second observation supporting this statement is that samples coated with 15 μm LSM had approximately the same parabolic rate constant as samples coated with 30 μm LSM. This means that the presence of the LSM coating does not affect the oxygen access at the surface of the growing oxide scale. A sketch of the likely diffusive fluxes in the oxide scale on LSM coated Crofer samples is presented in Fig. 9b.

The interface reactions taking place on the LSM coated Crofer samples are assumed to be similar to the interface reactions on the uncoated Crofer. However, at interface **III** the growing oxide scale also reacts with the LSM coating. The LSM coating contains 10% extra Mn, which at atmospheric pressure at 900 °C exists as Mn_2O_3. The $(La_{0.85}Sr_{0.15})MnO_3$ perovskite is stable under these conditions. A possible dissociation reaction for LSM is shown in Table 5 together with the change in Gibbs free energy. The reactions listed in Table 5 show that LSM is more stable than LSC and explain why the LSM particles do not decompose. Most likely, it is the Mn_2O_3 phase in the coating that reacts with the growing oxide scale, while the thermodynamically stable $(La_{0.85}Sr_{0.15})MnO_3$ perovskite particles are pushed ahead of the outwardly growing oxide scale (Fig. 3). The Mn_2O_3 are present as particles spread out in the LSM coating as illustrated in Fig. 9. The extra interface reaction in interface **III** is listed in Table 5.

The Mn content is approximately 17% higher in the outer spinel phase on the LSM coated samples than in the $MnCr_2O_4$ spinel phase found on uncoated Crofer sample. The extra uptake of Mn from the LSM coating leads to a decreased chromium content in the outer spinel phase compared to uncoated Crofer. The chromium content did however increase as oxidation proceeded, indicating continued outward chromium diffusion. The presence of the LSM coating also increased the spinel ratio in the oxide scale to approximately 40% in comparison to approximately 10% on uncoated Crofer. Furthermore, fewer metallic inclusions in the chromia layer on the LSM coated samples are observed compared to the uncoated samples. The increase of the relative thickness of the spinel layer would be consistent with a net flux of Cr species from spinel into coating and/or the contribution of Mn from the coating to spinel development. The thicker spinel layer on the LSM coated samples would reinforce the ability to hinder inward oxygen diffusion in the oxide scale. This reduces the overall oxidation rate and the oxidation process becomes more controlled by outward cation diffusion. The reduced number of metallic inclusions, which is indicative of the growth stresses at the chromia/alloy interface, in the coated samples is consistent with this hypothesis. Since the coating decreases the oxidation rate and the thickness of the oxide scale the smaller number of metal inclusions might also be explained by a decreased stress level in the oxide scale due to a thinner scale. However, the 4000 h sample of the LSM coated sample presents an oxide scale with about the same thickness (total oxide scale) as the oxide scale found on uncoated samples oxidized for 1000 h, but still the coated sample shows fewer metal inclusions which supports the first statement regarding a more dominant outward cation diffusion during oxidation.

In Fig. 9 the thermodynamically stable $(La_{0.85}Sr_{0.15})MnO_3$ particles are illustrated by black particles in zone D. During the initial stages of the oxidation these $(La_{0.85}Sr_{0.15})MnO_3$ particles will implement a geometrical protection against oxidation. The outwardly diffusing cations will be forced to diffuse an extra distance, x, along the particle to reach accessible gaseous oxygen (Fig. 9). The effect of the geometrical protection of the coating particles on the surface will slowly decrease as the thickness of the oxide scale grows larger and the diffusion through the oxide scale becomes the limiting diffusion distance, $(L_B + L_C) \gg x$.

4.6. Co_3O_4 coating

The Co_3O_4 coated samples showed a reduced oxidation rate compared to the uncoated samples. The positive effect of a porous Co_3O_4 coating on decreasing the oxidation rate of a Fe-22Cr alloy during oxidation at 900 °C has been reported before [41].

For the Co_3O_4 coated samples the spinel coating reacts with outwardly diffusing Cr- and Mn-cations and densifies [42]. In the very initial stage of oxidation the $Co_3O_4 \rightarrow CoO$ phase transition, that

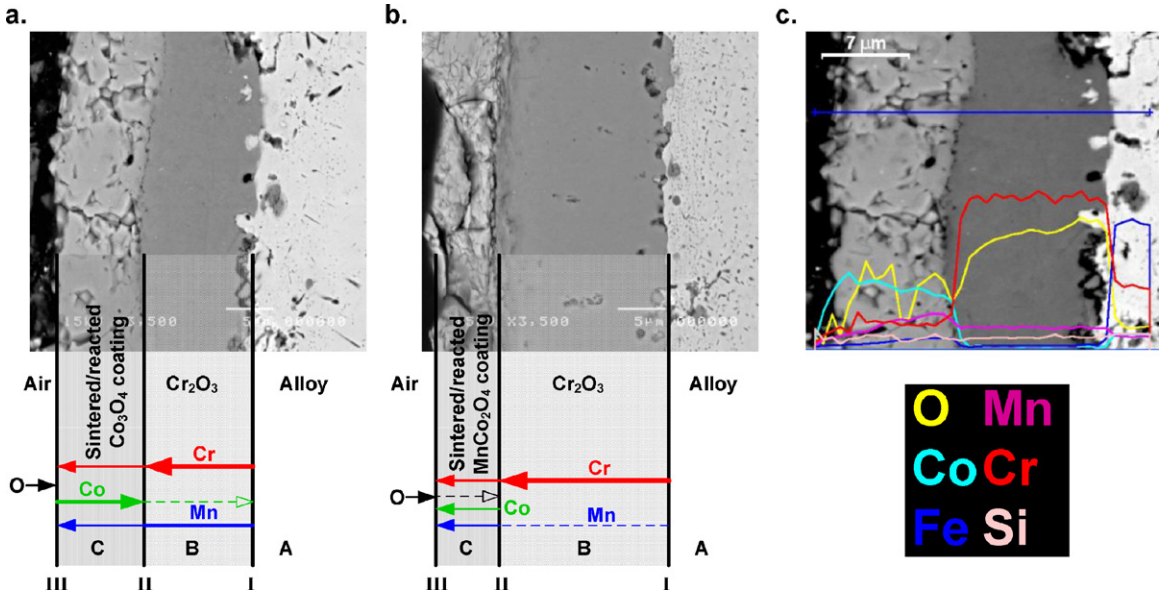

Fig. 10. Diffusive fluxes of ion during oxidation of (a) Co_3O_4 coated Crofer, (b) $MnCo_2O_4$ coated Crofer, and Line scan across the oxide scale and sintered/reacted Co_3O_4 coating (c) on micrographs of samples oxidized for 2000 h.

occurs around 900 °C [41,43–47], could probably play a role in the formation of a relatively dense structure, CoO does have a larger density than Co_3O_4 [48]. The coating particles restructure during the phase transition, which also could increase the reactivity of the particles towards the outwardly diffusing Cr- and Mn-cations due to the increased mobility in the cation-lattice. The oxide scale, established on the alloy surface due to oxidation will be interacting with a spinel phase during most of the oxidation process. This means that the interface reactions in the oxide scale for the Co_3O_4 coated Crofer samples are similar to the interface reactions summarized in Tables 4 and 5. But, in the spinel layer consisting of the formed spinel and the sintered/reacted residues of the Co_3O_4 coating EDS analysis shows that a concentration profile of Co is established, as seen in Fig. 10c. This concentration profile could indicate inward diffusion of Co in the spinel phase via cation vacancies, but is most likely an effect of dilution by Mn and Cr. It has been suggested in previous studies of Co_3O_4 coatings [13,49], that Co-cations might to some degree continue to diffuse into the chromia phase as illustrated via a dashed line in Fig. 10a, which is a sketch over the likely diffusive fluxes on the Co_3O_4 coated samples.

The 7 μm thick Co_3O_4 coating did not decrease the oxidation rate and the Cr-content in the outer oxide scale as much as the 15 μm thick Co_3O_4 coating (Tables 1a, 1b and 2). Clearly 7 μm is a too thin layer of Co_3O_4 coating to provide a durable protective effect at 900 °C.

4.7. $MnCo_2O_4$ coating

The $MnCo_2O_4$ coated samples show the same rate of parabolic oxidation behaviour as the uncoated samples; after 1000 h of oxidation break-away oxidation occurs. Just as for the Co_3O_4 coating, the $MnCo_2O_4$ coating appears to have sintered/reacted relatively dense already after 500 h. The diffusion and interface reaction conditions on the $MnCo_2O_4$ coated sample are the same as for the Co_3O_4 coated samples and assumed to be similar to the ones found on uncoated Crofer, albeit with some modifications. In Fig. 10b, a sketch of the diffusive fluxes in the oxidation process of $MnCo_2O_4$ coated samples is presented. The possible interface reactions on the $MnCo_2O_4$ coated samples are believed to be the same as those on uncoated samples supplemented by the **II**d interface reaction in Table 4.

In the micrographs in Fig. 4 a heavy edge oxidation after 2000 and 4000 h oxidation is visible on the $MnCo_2O_4$ coated samples, which explains the break-away oxidation behaviour observed after 1000 h oxidation in Fig. 1. EDS measurements show that the chromium content in the alloy next to these heavily oxidized areas drops well below 16 wt.% indicating depletion of chromium and oxidization of iron [24]. The observation of this heavy edge oxidation with significant iron content indicates that the accelerated oxidation is dominated by outward diffusion of iron.

Since the protective effects of the Co_3O_4 coating and the remarkable lack of protective effect of the $MnCo_2O_4$ coating were not completely understood based on the performed long-term oxidation experiments at 900 °C, additional experiments were conducted. A set of complementary oxidation experiments for uncoated, Co_3O_4 coated, and $MnCo_2O_4$ coated Crofer samples and Co_3O_4 coated YSZ-plates were performed at 900 °C in air containing 1% water for a total duration time of 1 h. The aim was to understand how fast the spinel coatings start to densify, and to find out whether the coatings would also densify on non-steel substrate. The results suggested that the reactivity of the Co_3O_4 coating with outwardly diffusing Cr- and Mn-ions from the Crofer alloy is crucial for the densification, and that the direct effect of the restructuring during the $Co_3O_4 \rightarrow$ CoO phase transition on the densification of the Co_3O_4 coating is of minor importance. The $MnCo_2O_4$ coating has undergone a slight densification after 1 h at 900 °C, but not to the same degree as the Co_3O_4 coating.

To study the effect of the spinel coatings on the oxidation rate of Crofer samples when all possible effects of the $Co_3O_4 \rightarrow$ CoO phase transition are eliminated, long-term oxidation of Co_3O_4 coated and $MnCo_2O_4$ coated Crofer sample was conducted in air containing 1% water at 850 °C. The chosen temperature is well below the phase transition temperature for Co_3O_4. The oxidation experiment was conducted in 250 h cycles and uncoated Crofer samples were also included. The total duration time for this experiment was 4000 h. In Fig. 11 the $(\Delta W/A)^2$–time plots for these samples are presented, and as for the results in Fig. 1 the first 250 h of oxidation was neglected.

The $(\Delta W/A)^2$–time plots of the uncoated, Co_3O_4 coated, and $MnCo_2O_4$ coated Crofer samples in Fig. 11 are linear indicating parabolic oxidation behaviour like at 900 °C. At 850 °C the uncoated samples do however show parabolic oxidation behaviour up to 4000 h without showing any break-away tendencies. The

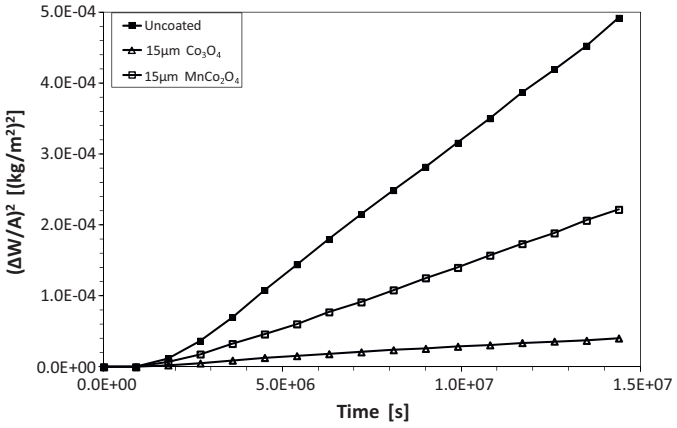

Fig. 11. The $(\Delta W/A)^2$–time plots for uncoated, Co_3O_4 coated and $MnCo_2O_4$ coated Crofer 22APU samples in the long-term, cyclic oxidation experiment carried out at 850 °C in air containing 1% water for a total of 4000 h.

Table 6
Parabolic rate constants for uncoated, Co_3O_4 coated, and $MnCo_2O_4$ coated Crofer samples estimated from the 4000 h oxidation at 900 °C and 850° in air containing 1% water, the weight gain from the first 250 h is neglected.

900 °C		
	k_p [kg^2 m^{-4} s^{-1}]	Time [h]
Uncoated	$(8.2 \pm 2.5) \times 10^{-11}$	1000
15 μm Co_3O_4	$(1.7 \pm 0.6) \times 10^{-11}$	2750
	4.4×10^{-11}	3000–4000
15 μm $MnCo_2O_4$	$(9.4 \pm 1.5) \times 10^{-11}$	1250
850 °C		
Uncoated	$(3.4 \pm 0.5) \times 10^{-11}$	4000
15 μm Co_3O_4	$(0.3 \pm 0.03) \times 10^{-11}$	4000
15 μm $MnCo_2O_4$	$(1.4 \pm 0.2) \times 10^{-11}$	4000

Co_3O_4 coating decreases the growth rate of the oxide scale, just as observed at 900 °C (Fig. 1). The $MnCo_2O_4$ coating does appear to decrease the oxidation rate compared to an uncoated sample at 850 °C, unlike at 900 °C where no protective effect of the $MnCo_2O_4$ coating was observed (Fig. 1). The $MnCo_2O_4$ coated sample does not experience any break-away oxidation during oxidation at 850 °C. From Figs. 2–4 and Tables 1a and 1b it appears that during oxidation at 900 °C break-away oxidation occurs when the oxide scale has grown 10–15 μm thick. The Co_3O_4 coated samples present thicker oxide scales than 10–15 μm (just grown Cr_2O_3) (Tables 1a and 1b). This can be explained by the coating being able to change the stress-distribution in the grown oxide scale, and avoiding break-away conditions at the detrimental 10–15 μm and even thicker oxide scales. As seen in Fig. 12, the oxide scales on the uncoated, Co_3O_4 coated, and $MnCo_2O_4$ coated Crofer samples had not reached the detrimental 10–15 μm thickness after 2000 h oxidation at 850 °C.

In Table 6 the parabolic rate constants for the uncoated, Co_3O_4 coated, and $MnCo_2O_4$ coated samples oxidized at 850 °C are listed together with corresponding parabolic rate constants at 900 °C from Tables 1a and 1b.

Comparing the oxidation rates of the samples oxidized at 850 °C and 900 °C it is found that the Co_3O_4 coating lowers the parabolic rate constant with 92% at 850 °C and 80% at 900 °C (Tables 1a and 6). That is, the effect of the Co_3O_4 coating appears similar at the two temperatures. The $MnCo_2O_4$ coating on the other hand lowered the parabolic rate constant with 60% at 850 °C but increased it with 13% at 900 °C. The temperature obviously affects the effect of the $MnCo_2O_4$ coating.

Conclusive evidence to explain why a spinel coating is successful in decreasing the oxidation rate of the scale when the spinel coating consists of Co_3O_4, but unsuccessful when it consists of $MnCo_2O_4$, was not found in this study. The following five factors are important for the effect of the coating on the corrosion:

1. the chemical potential gradient of Mn and Cr, $\Delta\mu_{Mn/Cr}$, established across the Cr_2O_3 scale;
2. the density, ρ, of the formed spinel phase;
3. the number of grain boundaries in the formed spinel phase;
4. the effective diffusion coefficients for Mn-, Cr-, Co-, and O-ions through the formed spinel phase;
5. the reactivity of the spinel coating with the outwardly diffusing Mn-, and Cr-ions.

Both the Co_3O_4 and the $MnCo_2O_4$ coated sample originally had the same concentration profile of Cr across the chromia layer, therefore is not considered a reliable explanation. The gradient leading to outward diffusion of Mn is smaller for the $MnCo_2O_4$ coated samples; however, as this sample oxidizes faster it is apparently not rate determining for the oxidation rate.

Based on the micrographs in Figs. 3 and 4 it is difficult to observe any significant difference in relative density of the sintered/reacted Co_3O_4 and $MnCo_2O_4$ coatings and the number of grain boundaries in the two reacted/sintered coatings. However, one cannot rule out that such a difference does exist and is the reason for the very different protective performances of the two coatings.

It is possible that the Mn- and Co-cations in the spinel phase on the $MnCo_2O_4$ coated samples have a significantly higher mobility than Co-cations in Co_3O_4, or that the number of cation vacancies is larger in the former. This results in a larger effective inward oxygen diffusion, as a consequence of the cation vacancy transport (reactions **II**a and **III**a, Table 4), and feeds the growth of the chromia phase underneath. Alternatively, in terms of ionic species, Mn- and Co-cations diffuse outwardly towards the oxide surface as illustrated in Fig. 10.

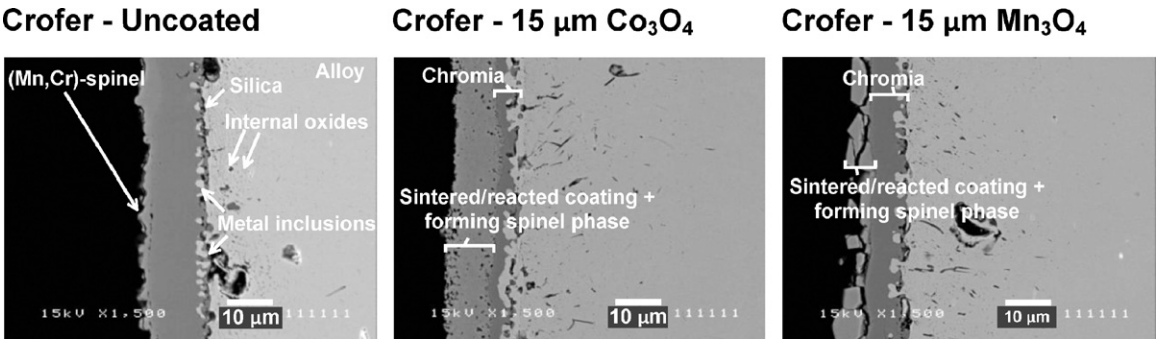

Fig. 12. BSE micrographs of the polished cross-sections of uncoated, 15 μm Co_3O_4 coated, and 15 μm $MnCo_2O_4$ coated Crofer oxidized for 2000 h at 850 °C in air containing 1% water.

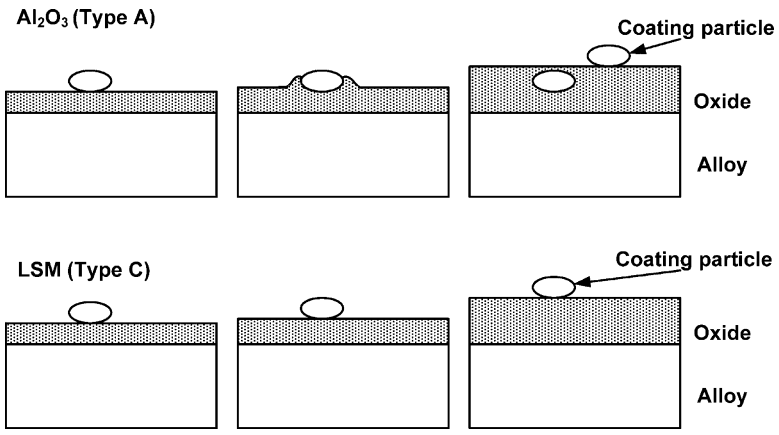

Fig. 13. Sketch of incorporation process of coating particles, like Al_2O_3, and the case where the coating particle is pushed in front of the growing oxide scale, e.g. LSM.

The reactivity of the Co_3O_4 and $MnCo_2O_4$ coatings with the outwardly diffusing Mn-, and Cr-ions would affect the microstructure of the sintered/reacted spinel coating. According to a calculation of the Gibbs energy change, ΔG, from a mechanical mixture of Cr_2O_3, Mn_3O_4 and CoO to the equilibrium state at 900 °C, calculated using the FactSage Thermochemical Software and Databases, see Appendix A, the thermodynamic driving force for the reaction (ΔG) is larger the lower the Mn content is in the mixture. This may explain why the Co_3O_4 coating is more reactive than the $MnCo_2O_4$ coating, and therefore provides a better protection against oxidation.

The significant protective action of the Co_3O_4 observed also at 850 °C shows that the clear difference in protective action between $MnCo_2O_4$ and Co_3O_4 observed at 900 °C, see Figs. 1 and 11 and Table 6, does not lie in the phase change $Co_3O_4 \rightarrow CoO$ occurring at 900 °C, which is absent for $MnCo_2O_4$. The difference in protective ability lies in the reaction occurring between outwardly diffusing Cr- and Mn-ions, and the Co_3O_4 coating results in (a) either a more gas tight microstructure facilitated by the larger reactivity of this coating, or (b) a spinel phase with significantly slower cation conductivity than for the $MnCo_2O_4$ coating.

5. Summary and conclusion

Five out of the six included coatings in this study decreased the oxidation rate of Crofer 22APU. Only the $MnCo_2O_4$ coating did not decrease the weight gain of the oxidized samples oxidized at 900 °C. Four out of six of the coatings, Co_3O_4, $MnCo_2O_4$ ($(La_{0.85}Sr_{0.15})_{1-x}Mn_{1+x}O_3 + (0.1-x)Mn_2O_3$, and $(La_{0.85}Sr_{0.15})CoO_3$ + 10 wt.% Co_3O_4, affected the composition of the outer oxide scale, whereas Al_2O_3 and ZrO_2 did not change the outer oxide scale composition compared to the uncoated samples. However, the spinel/chromia ratio in the oxide scale increased.

Three different interaction mechanisms between the applied coatings and the forming oxides were identified:

Al_2O_3 and ZrO_2: Coating particles are incorporated in the growing oxide scale;
Co_3O_4 and $MnCo_2O_4$: Sinter/react with the growing oxide scale;
LSC: Partially incorporated and reacting with the growing oxide scale, while main part of the coating remains porous;
LSM: Remains porous and is pushed in front of the growing oxide scale while simultaneously adding elemental addition to the growing oxide scale.

In Al_2O_3 and ZrO_2 coated samples, coating particles are incorporated into the growing oxide scale, see Fig. 13, and function as a geometrical cation barrier. There is no chemical change of the naturally forming $MnCr_2O_4$. The spinel ratio in the oxide scale is however increased in the presence of the Al_2O_3 and ZrO_2 coatings (Table 3). The incorporation of chemically stable coating particles in the oxide scale would take place if the interface energy of the coating particle/oxide scale-interface is lower than the total surface energy of the growing oxide scale and the coating particle.

In Co_3O_4 and $MnCo_2O_4$ coated Crofer samples the Co_3O_4 and $MnCo_2O_4$ coatings sinter/react dense at high temperature oxidation when interacting with Crofer 22APU. However, the Co_3O_4 coating is successful in decreasing the oxidation rate while the $MnCo_2O_4$ coating is not at 900 °C. The difference in protective ability between the $MnCo_2O_4$ and Co_3O_4 coatings could at this stage best be explained by the spinel phase formed in the presence of the Co_3O_4 coating having a more gas tight microstructure or a much slower Cr/Mn conductivity than the spinel phase formed in the presence of a $MnCo_2O_4$ coating.

The LSC coating is partially dissociated into $LaCrO_3$, $SrCrO_4$ and (Co,Cr,Mn)-spinel that all three are incorporated into the growing oxide scale during oxidation. The incorporated $LaCrO_3$ and $SrCrO_4$ particles will function as a geometrical diffusion barrier as in the case of the interaction mechanism type A (Fig. 13). The LSC coating will also function as a Co-source for the growing oxide scale, and increase the Co-content in the spinel phase. The main part of the LSC coating remains porous.

The LSM coating is a Mn-source for the growing oxide scale and shifts the naturally forming $MnCr_2O_4$ spinel towards a higher Mn content. The coating remains porous and is pushed ahead of the growing oxide scale (Fig. 13).

For SOFC applications a bias current will be drawn across the oxide scales formed on both the cathode side (studied in this paper) and on the anode side of the interconnect. The externally applied electrical field increases the outward diffusion of Cr^{3+}-ions on the anode side and decreases the outward Cr^{3+} diffusion on the cathode side. However, since the formed oxide scale in this case has a fairly good electronic conductivity in comparison to its ionic conductivity the effect of the bias current is small in this case [24].

Out of the six coatings the LSC coating provided the best corrosion protection.

An optimal coating would probably consist of a combination of all three interaction mechanisms. Out of the six coatings compared in this study LSC presented the best protection against corrosion, and as described above LSC also have multiple interaction mechanisms with the growing oxide scale.

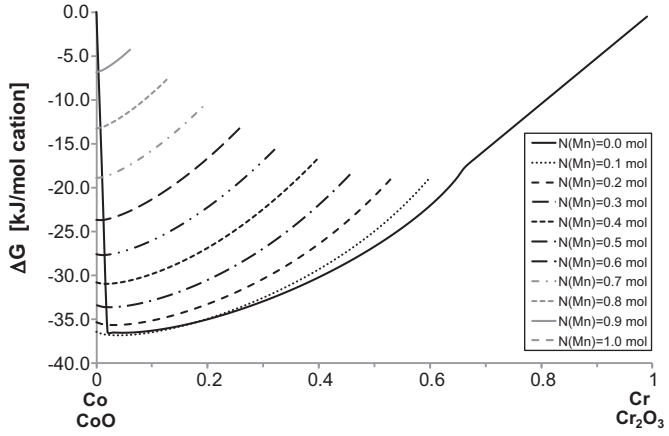

Fig. A.1. The plots of the Gibbs energy change, ΔG, from a mechanical mixture of Cr_2O_3, Mn_3O_4 and CoO to the equilibrium state at 900 °C calculated using the FactSage Thermochemical Software and Databases, where the composition of the system was set as $x1/2Cr_2O_3 + (1 - x - N)CoO + N1/3Mn_3O_4$, where the number of mole Mn-cation, N, Cr-cations, x, and Co-cations, $(1 - x - N)$ are related to each other assuming the total number of mole cations should be 1.0 [21].

Acknowledgements

This work was financially supported by Energinet.dk project no. 2006-1-6342.Dr. Ming Chen performed the thermodynamic calculations included in this paper, and Dr. Ruth Knibbe performed the TEM analysis.

Appendix A. Calculation of ΔG

A calculation of the Gibbs energy change, ΔG, from a mechanical mixture of Cr_2O_3, Mn_3O_4 and CoO to the equilibrium state at 900 °C, was done using the FactSage Thermochemical Software and Databases and is presented in Fig. A.1 [21]. The composition of the system was set as $x1/2Cr_2O_3 + (1 - x - N)CoO + N1/3Mn_3O_4$,where the number of moles Mn-cations, N, can be related to the number of moles Cr-cations, x, and Co-cations, $(1 - x - N)$ if the total number of mole cations was assumed to be 1.0. The more negative the ΔG is, the larger is the thermodynamic driving force for a reaction between the three species. A large negative ΔG does not necessarily imply that the reaction to form this oxide proceeds fastest, however it is likely.

From the plots in Fig. A.1 it is seen that the thermodynamic driving force for the reaction (ΔG) is larger the lower the Mn content is in the mixture.

References

[1] S.C. Singhal, K. Kendall, High Temperature Solid Oxide Fuel Cells Fundamentals, Design and Applications, Elsevier, Cornwall, 2003.
[2] W.J. Quadakkers, J. Piron-Abellan, V. Shemet, L. Singheiser, Mater. High Temp. 20 (2003) 115–127.
[3] S. Linderoth, P.V. Hendriksen, M. Mogensen, N. Langvad, J. Mater. Sci. 31 (1996) 5077–5082.
[4] J.W. Fergus, Mat. Sci. Eng. A—Struct. 397 (2005) 271–283.
[5] E. Konysheva, H. Penkalla, E. Wessel, J. Mertens, U. Seeling, L. Singheiser, K. Hilpert, J. Electrochem. Soc. 153 (2006) A765–A773.
[6] M.C. Tucker, H. Kurakawa, C.P. Jacobson, L.C. De Jonghe, S.J. Visco, J. Power Sources 160 (2006) 130–138.
[7] Y. Matsuzaki, I. Yasuda, Solid State Ionics 132 (2000) 271–278.
[8] Z.G. Yang, J.S. Hardy, M.S. Walker, G.G. Xia, S.P. Simner, J.W. Stevenson, J. Electrochem. Soc. 151 (2004) A1825–A1831.
[9] M. Stanislowski, E. Wessel, K. Hilpert, T. Markus, L. Singheiser, J. Electrochem. Soc. 154 (2007) A295–A306.
[10] S.P. Simner, M.D. Anderson, G.G. Xia, Z. Yang, L.R. Pederson, J.W. Stevenson, J. Electrochem. Soc. 152 (2005) A740–A745.
[11] K. Huang, P.Y. Hou, J.B. Goodenough, Mater. Res. Bull. 36 (2001) 81–95.
[12] Zahid M., Tietz F., Sebold D., Buchkremer H.P., Reactive Coatings agains Chromium Evaporation in Solid Oxide Fuel Cells, Proceedings of the European SOFC Forum 2004 (2004), pp. 820–827.
[13] A.N. Hansson, S. Linderoth, M. Mogensen, M.A.J. Somers, J. Alloy Compd. 433 (2007) 193–201.
[14] T. Kadowaki, T. Shiomitsu, E. Matsuda, H. Nakagawa, H. Tsuneizumi, T. Maruyama, Solid State Ionics 67 (1993) 65–69.
[15] Z.G. Yang, G.G. Xia, J.W. Stevenson, Electrochem. Solid-State Lett. 8 (2005) A168–A170.
[16] M.R. Bateni, P. Wei, X.H. Deng, A. Petric, Surf. Coat. Tech. 201 (2007) 4677–4684.
[17] Y. Larring, T. Norby, J. Electrochem. Soc. 147 (2000) 3251–3256.
[18] W.Z. Zhu, S.C. Deevi, Mater. Res. Bull. 38 (2003) 957–972.
[19] S. Linderoth, Surf. Coat. Tech. 80 (1996) 185–189.
[20] X. Chen, P.Y. Hou, C.P. Jacobson, S.J. Visco, L.C. De Jonghe, Solid State Ionics 176 (2005) 425–433.
[21] Calculated using FactSage 5.5,1-5-2007.
[22] M. Sogaard, P.V. Hendriksen, M. Mogensen, F.W. Poulsen, E. Skou, Solid State Ionics 177 (2006) 3285–3296.
[23] K. Kitazawa, R.L. Coble, J. Am. Ceram. Soc. 57 (1974) 245–250.
[24] P. Kofstad, High Temperature Corrosion, Elsevier Applied Science Publishers LTD, 1988.
[25] M. Kuznecov, K. Eichler, S. Megel, P. Otschik, Proceedings of the European SOFC Forum 2004 (2004) 1573–1585.
[26] Z.G. Yang, G.G. Xia, P. Singh, J.W. Stevenson, J. Power Sources 155 (2006) 246–252.
[27] J.E. Hammer, S.J. Laney, R.W. Jackson, K. Coyne, F.S. Pettit, G.H. Meier, Oxid. Met. 67 (2007) 1–38.
[28] V.K. Tolpygo, D.R. Clarke, Acta Mater. 46 (1998) 5153–5166.
[29] H. Schmalzried, Chemical Kinetics of Solids, VCH Verlagsgesellschaft mbH, Weinheim, 1995.
[30] P. Huczkowski, N. Christiansen, V. Shemet, L. Niewolak, J. Piron-Abellan, L. Singheiser, W.J. Quadakkers, Fuel Cells 6 (2006) 93–99.
[31] A.C.S. Sabioni, A.M. Huntz, L.C. Borges, F. Jomard, Philos. Mag. 87 (2007) 1921–1937.
[32] R.E. Lobnig, H.P. Schmidt, K. Hennesen, H.J. Grabke, Oxid. Met. 37 (1992) 81–93.
[33] P. Kofstad, Defects, Oxid. Met. 44 (1995) 3–27.
[34] R. Dieckmann, J. Phys. Chem. Solids 59 (1998) 507–525.
[35] J. Topfer, S. Aggarwal, R. Dieckmann, Point-Defects, Solid State Ionics 81 (1995) 251–266.
[36] F.H. Lu, S. Tinkler, R. Dieckmann, Point-Defects, Solid State Ionics 62 (1993) 39–52.
[37] F.H. Lu, R. Dieckmann, Point-Defects, Solid State Ionics 53-6 (1992) 290–302.
[38] F.H. Lu, R. Dieckmann, Point-Defects, Solid State Ionics 59 (1993) 71–82.
[39] F.H. Lu, R. Dieckmann, Solid State Ionics 67 (1993) 145–155.
[40] A.N. Hansson, M.A.J. Somers, Proceedings of the 6th International Conference on the Microscopy of Oxidation (2005) 49–55.
[41] A.N. Hansson, Ph.D. Thesis, Oxides in the Co—Cr—Fe—O system and oxidation behaviour of coated Fe-22Cr steel, 2004.
[42] D.L. Douglass, J.S. Armijo, Oxid. Met. 3 (1971) 185–202.
[43] J. Jankowski, G. Thomas, L.P. Camby, Solid State Ionics 101 (1997) 1321–1326.
[44] G.M. Kale, S.S. Pandit, K.T. Jacob, Mater. T JIM 29 (1988) 125–132.
[45] H.S.C. Oneill, Phys. Chem. Miner. 12 (1985) 149–154.
[46] L. Xing, C.T. Prewitt, Phys. Chem. Miner. 17 (1990) 168–172.
[47] O.M. Sreedharan, M.S. Chandrasekharaiah, M.D. Karkhanavala, High Temp. Sci. 9 (1977) 109–118.
[48] David R. Lide (Ed.), CRC Handbook of Chemistry and Physics, 85, CRC Press LLC, New York, 2004.
[49] K.Q. Huang, P.Y. Hou, J.B. Goodenough, Solid State Ionics 129 (2000) 237–250.